Distributed Current Source Method for Modeling Magnetic and Eddy-Current Fields induced in Biological Object

Chun-Yeon Lin, *Member, IEEE/ASME*; Kok-Meng Lee, *Fellow, IEEE/ASME*; Yuan-Liang Chen; Shih-Cheng Huang

***Abstract*—This paper presents a distributed current source method for modeling weak magnetic and eddy-current (EC) fields induced in biological objects for electromagnetic stimulation and sensing applications. Unlike metallic objects with negligible displacement currents, the permittivity must be accounted for in biological objects. An axial symmetrical 2D EC field induced in a biological object is formulated in state space representation. Since EC fields cannot be directly measured, the solutions to three different variables that provide a means to infer the EC effects are derived using the distributed current source method, which are the magnetic flux density generated by the induced EC at a point, the lumped-parameter magnetic flux passing through a sensing coil, and its electromotive force. Illustrated in the context of two applications, the solutions are numerically evaluated by comparing results with that simulated by a commercial finite-element analysis.**

I. Introduction

Magnetic/eddy-current (M/EC) devices play an important role as actuators and/or sensors in a broad spectrum of applications ranging from manufacturing to biomedical engineering. In manufacturing, M/EC actuators have been employed on vibration suppression [1][2], induction heat [3][4]. M/EC sensors have been widely used in measurements of displacement [5][6], thickness [7], electrical conductivity [8] and recently, simultaneous geometrical/material- property measurements [9]. As a non-invasive neuro- modulation technique, transcranial magnetic stimulation (TMS) has been used to treat and diagnosis some psychiatric disorder (such as Alzheimer's and Parkinson's disease), which induces an electric field in a specific region that is conductive of the brain and causes a localized axial depolarization having positive effects for aforementioned disorders in the cortical tissue [10] [11]. Magnetic induction tomography (MIT) [12] is an electrodeless technique through the use of excitation coils to induce an electromagnetic field in the material, which is measured at the receiving side by sensors. This noninvasive modality that applies an electromagnetic field is sensitive to all three passive electromagnetic properties (electrical conductivity, permittivity, and permeability) in tissues. MIT applications include lung monitoring and imaging [13], brain imaging [14], liver tissue monitoring [15], to name a few. Because EC fields cannot be directly measured, their effects are determined by measuring the magnetic flux density (MFD) generated by the induced EC at a point, the lumped-parameter magnetic flux (MF) passing through a sensing coil, or its corresponding electromotive force (EMF). Thus, the design of M/EC devices requires a good understanding and physics-based modeling of the M/EC fields involved.

In [16], analytical solutions were derived for axisymmetric EC induced by a coil in a semi-infinite conducting slab. Built upon the flexible division algorithm that formulates a physical field in state space [17] and the distributed multi-level current modeling method [18] that accounts for mutual induction in a conductor, a distributed current source (DCS) method was presented in [19] to model the harmonic EC field induced in a nonferrous metal and its corresponding magnetic flux density. Different from metallic objects, the effects of displacement currents and permittivity in biological objects cannot be neglected. The modeling of EC induced in biological tissues can be broadly classified into lumped-parameter and distributed-parameter approaches. The lumped-parameter approach, typically known as impedance method (IM) [20] [21] and independent impedance method (IIM) [22][23], subdivides the object into a network of impedances for electromagnetic stimulation. Both IM and IIM methods focus on solving the EC induced in excited objects during electromagnetic stimulation, and do not calculate the weak magnetic field generated from the biological tissues. Finite element analysis (FEA) methods (capable of handling complex geometries when solving the partial differential equations of a physical field) have been most commonly used to calculate the EC induced in the biological object and its MFD; the latter was solved by subtracting the MFD generated by the combined electromagnet (EM) and biological objects from that solely by the external EM (without the biological object). Because biological objects typically characterized by the relatively small electrical conductivity, the MFD generated by the EC induced in the biological object is much smaller than that from the EM; as a result, the FEA methods that base on the subtraction two MFD fields (with and without the biological object) cause significant errors in computation. Furthermore, because of the weak MFD generated by the EC induced in a biological object, a sensing coil is often utilized in bio-electromagnetic sensing applications.

Motivated by the interests to compute the MFD generated by the EC induced in biological objects and its corresponding magnetic flux (MF) and electromotive force (EMF), the DCS method [19] for non-ferrous metallic objects is further

This work was supported by Ministry of Science and Technology, Taiwan, under Grant MOST 108-2218-E-002-038-MY2, U. S. National Science Foundation under Grants EFRI-M3C 1137172 and CMMI-1662700.

C.-Y. Lin*, Y.-L. Chen and S.-C. Huang are with the Department of Mechanical Engineering, National Taiwan University, No. 1, Sec. 4, Roosevelt Road, Taipei, 10617, Taiwan.

K. -M. Lee* is with the George W. Woodruff School of Mech. Eng. at Georgia Inst. of Tech., Atlanta, GA 30332 USA. K.-M. Lee is also Distinguished Professor of the State Key Lab. of Dig. Manuf. Equip. and Tech. and Sch. of Mech. Sci. and Eng. at Huazhong Univ. of Sci. and Tech., Wuhan, Hubei, 430074, P. R. China.

* *Corresponding authors:* kokmeng.lee@me.gatech.edu.

Manuscript 408 submitted to IEEE/ASME International Conference on Advanced Intelligent Mechatronics. Received March 15, 2019.

developed to relax for biological objects by considering the permittivity. As a result, the first-order state-space model of the non-ferrous metallic objects becomes second-order. In this paper, the MF passing through and EMF generated in the sensing coil are formulated as outputs of the dynamics M/EC models. The remainder of this paper provides the following:

- The next section begins with an extended version of the distributed current source (DCS) method to model the M/EC fields in a 2D axisymmetric biological object for magnetic stimulation applications. The biological object stimulated by an external EM is discretized into elements for state-space formulation of the M/EC fields with the EC density (ECD) of the distributed elements as state variables, current density passing through the EM and its time derivative as inputs. The distributed EC-induced MFD at a point and the lumped-parameter MF and EMF of a sensing coil are formulated as outputs. The closed-form harmonic solutions are derived.
- Illustrated with two examples, the DCS method for modeling the ECD induced in a biological object is numerically evaluated by comparing results with FEA simulations. As will be demonstrated, the DCS method overcomes some problems encountered in FEA that lacks of the ability to calculate the MFD generated from the tiny ECDs induced in the biological object and the large differences between the EM-generated MFD and the EC-generated MFD by the biological objects.

II. DCS-BASED EC MODEL IN BIOLOGICAL OBJECTS

Figure 1(a) illustrates an ECD field induced in a biological object (tissues) by a time-varying current $I(t)$ with an average value I_o flowing through the EM (N_e-turn coil), where the parameters involved in the 2D axis-symmetrical model are defined in cylindrical coordinates (r, z). In Fig. 1(a), (a_i, a_o; a) are the (inner, outer radii; half-length) of the EM. For modeling using a DCS method, the object is decomposed into n_l layers of n elemental biological tissues with the i^{th} element characterized by its geometrical/material properties (surface area v_i, electrical conductivity σ_i, permittivity ε_i).

A. Governing Equations

The induced ECD field governed by the Maxwell's equations is solved in terms of a magnetic vector potential $\boldsymbol{\varphi}$ ($=\boldsymbol{\varphi}_E+\boldsymbol{\varphi}_C$), where $\boldsymbol{\varphi}_E$ and $\boldsymbol{\varphi}_C$ are the contributions from the EM and the mutual inductance among the elemental conducting issues respectively:

$$\mathbf{J} = -\left(\sigma + \dot{\varepsilon} + \varepsilon\frac{\partial}{\partial t}\right)\frac{\partial(\boldsymbol{\varphi}_E + \boldsymbol{\varphi}_C)}{\partial t} \tag{1a}$$

In (1a), the complex permittivity and conductivity (ε, σ) are frequency-dependent electrical properties of the bio-materials given in (1b, c) where ε_0 ($=8.852\times10^{-12}$ F/m) is the permittivity of free space, ε_∞ is the permittivity in the high frequency limit and σ_I is the static ionic conductivity:

$$\frac{\varepsilon(\omega)}{\varepsilon_0} = \varepsilon_\infty(\omega) + \sum_{n=1}^{4}\frac{\Delta\varepsilon_n}{1+(j\omega\tau_n)^{1-\alpha_n}} - j\frac{\sigma_I}{\omega\varepsilon_0} \tag{1b}$$

$$\sigma(\omega) = -\omega\varepsilon_{\mathrm{Im}}(\omega) \tag{1c}$$

The dielectric spectrum of biological tissues in (1b) where $\Delta\varepsilon_n$, τ_n and α_n are appropriately chosen to each tissue is described by the multiple Cole-Cole dispersion [24][25]. In (1c), $\varepsilon_{\mathrm{Im}}$ is the imaginary part of relative permittivity.

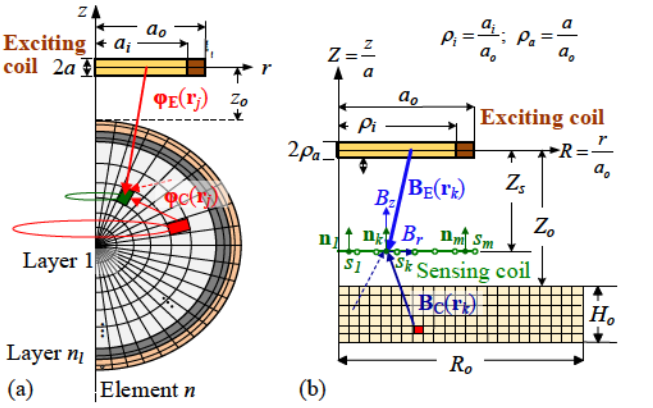

Fig. 1 Schematics showing variables/parameters in the formulation. (a) Electromagnetic stimulation. (b) Electromagnetic sensing.

Using the Biot-Savart's law [26], $\boldsymbol{\varphi}_E(\mathbf{r}_j, t)$ contributed by the current density $J_E(t)$ flowing through the exciting EM can be determined from (2) where μ_0 ($=4\pi\times10^{-7}$H/m) is the magnetic permeability of free space:

$$\boldsymbol{\varphi}_E(\mathbf{r}_j, t) = \frac{\mu_o}{4\pi}\int_{\theta=0}^{2\pi}\int_{z=-a}^{a}\int_{r=a_i}^{a_o}\frac{\mathbf{e}_\theta J_E(t)}{|\mathbf{r}_j-\mathbf{r}'|}r\,dr\,dz\,d\theta \tag{2}$$

In dimensionless form with normalized coordinates ($R=r/a_o$, $Z=z/a$, θ), $\boldsymbol{\varphi}_E$ can be written in terms of an integral $\boldsymbol{\gamma}_E(\mathbf{r}_j)$ and EM geometry ($\rho_i=a_i/a_o$ and $\rho_a=a/a_o$), where J_o is the uniform current density of the unit input current, $I_E(t)$ is the current intensity, and N_E is the number of turns:

$$\frac{\boldsymbol{\varphi}_E(\mathbf{r}_j, t)}{\mu_o} = \boldsymbol{\gamma}_E(\mathbf{r}_j)J_E(t);\ J_E(t) = J_0 I_E(t);\ J_0 = \frac{N_E}{a_o a} \tag{3a}$$

$$\boldsymbol{\gamma}_E(\mathbf{r}_j) = \frac{aa_o}{4\pi}\int_{\theta=0}^{2\pi}\int_{Z=-1}^{1}\int_{R=\rho_i}^{1}\frac{\mathbf{e}_\theta R dR\,dZ d\theta}{|\mathbf{R}-\mathbf{R}_j|};\ \text{and} \tag{3b}$$

$$|\mathbf{R}-\mathbf{R}_j| = \sqrt{(R-R_j\cos\theta)^2+(R_j\sin\theta)^2+\rho_a^2(Z-Z_j)^2} \tag{3c}$$

In 2D axisymmetric coordinates, $\boldsymbol{\varphi}_C$ is the sum of all the n elemental magnetic vector potentials contributed by the mutual inductance among the elements in the rings

$$\frac{\boldsymbol{\varphi}_C(\mathbf{r}_j)}{\mu_o J_o} = \sum_{i=1}^{n}\left(\gamma_{cji}\frac{v_i}{a_o^2}\frac{\mathbf{j}_i}{J_o}\right) \tag{4a}$$

$$\gamma_{cij} = \frac{1}{4\pi}\int_0^{2\pi}\frac{\cos\theta}{f(\theta)}d\theta \text{ where } f(\theta) = \begin{cases}2(R-\cos\theta) & i=j\\ |\mathbf{r}_j-\mathbf{r}'|/a_o & i\neq j\end{cases} \tag{4b}$$

In (4a, b) where quadrilateral elements are assumed, the double subscript ij indicates that the j^{th} magnetic vector potential is contributed by the i^{th} elemental ECD source j_i.

As EC cannot be directly measured, its effects are inferred by one of the three following methods:

1. The magnetic flux density $\mathbf{B}$ ($=\mathbf{B}_E+\mathbf{B}_C$) generated by the combined EM and EC induced in the conductor at a point can be derived from the curl of $\boldsymbol{\varphi}$ leading to

$$\mathbf{B}(\mathbf{r}) = \frac{\mu_0}{4\pi}\int_\Omega\frac{\mathbf{J}(\mathbf{r}')\times(\mathbf{r}-\mathbf{r}')}{|\mathbf{r}-\mathbf{r}'|^3}dV \tag{5a}$$

2. The magnetic flux Φ_B (unit: W_b or Tm^2) can be determined by integrating the B over a cross-sectional area S:

$$\Phi_{\mathrm{B}}=\iint_{s}\mathbf{B}\cdot d\mathbf{S} \tag{5b}$$

3. The induced electromotive force (EMF) V_b sensing coil can be determined by the Faraday's law in (5c) where N_w is the number of turns in the coil:

$$V_b=-N_w\frac{d\Phi_{\mathrm{B}}}{dt} \tag{5c}$$

B. Distributed-Parameter State-Space Formulation

Using the DCS method, the ECD **J** of the distributed-parameter system (1) can be expressed in terms of its elemental ECD sources, $\mathbf{J}=\begin{bmatrix}\mathbf{j}_1 & \cdots & \mathbf{j}_i & \cdots & \mathbf{j}_n\end{bmatrix}^{\mathrm{T}}$. For the discretized 2D axisymmetric system, the j^{th} elemental ECD in the tangential direction can be determined in (6):

$$-\mathbf{j}_j=\mu_0\left(\sigma_j+\dot{\varepsilon}_j+\varepsilon_j\frac{d}{dt}\right)\sum_{i=1}^{n}\left(\gamma_{cji}v_i\frac{d\mathbf{j}_i}{dt}+\boldsymbol{\gamma}_{\mathbf{E}j}\frac{dJ_E}{dt}\right) \tag{6}$$

Each of the elemental ECD must obey the law of energy conservation referred to here as the continuity equation and boundary conditions, which are automatically satisfied for a 2D axis-symmetrical model. The variables of interests in (6) can be expressed in matrix forms (7a~ c) where (**X**, **U** and **Y**) are the (state, input and output) vectors:

State vector: $$\mathbf{X}\left(\in\mathbb{R}^{2n\times1}\right)=\begin{bmatrix}\mathbf{J}\\ \dot{\mathbf{J}}\end{bmatrix} \tag{7a}$$

Input vector: $$\mathbf{U}\left(\in\mathbb{R}^{3\times1}\right)=\begin{bmatrix}J_E\\ \dot{J}_E\\ \ddot{J}_E\end{bmatrix} \tag{7b}$$

output vectors: $$\mathbf{Y}_1\left(\in\mathbb{R}^{2\times1}\right)=\begin{bmatrix}B_r\\ B_z\end{bmatrix} \tag{7c}$$

$$Y_2=\Phi_{\mathrm{B}} \tag{7d}$$

$$Y_3=V_b \tag{7d}$$

Using (6) and the definitions (7a, b), (6) is represented in state space with specified parameters,

$$\left[\mathbf{A}_{\mathbf{C}}(i,j)\right]=v_j\gamma_{cij}(t)=v_j\gamma_{cji}(t);$$

$$\left[\mathbf{A}_{\mathbf{E}}(j)\right]=\begin{bmatrix}\boldsymbol{\gamma}_{\mathbf{E}1} & \cdots & \boldsymbol{\gamma}_{\mathbf{E}j} & \cdots & \boldsymbol{\gamma}_{\mathbf{E}n}\end{bmatrix}^{\mathrm{T}};$$

$$\mathbf{E}_{\mathrm{p}}=diag(\mu_0\varepsilon_j),\quad \mathbf{S}=diag(\mu_0\sigma_j)$$

the "*diag*" denotes a diagonal matrix with scalar elements (j=1,…, n):

$$\dot{\mathbf{X}}=\begin{bmatrix}\mathbf{0}_{n\times n} & \mathbf{1}_{n\times n}\\ \boldsymbol{\alpha}_1 & \boldsymbol{\alpha}_2\end{bmatrix}\mathbf{X}+\begin{bmatrix}\mathbf{0}_{n\times1} & \mathbf{0}_{n\times1} & \mathbf{0}_{n\times1}\\ \mathbf{0}_{n\times1} & \boldsymbol{\beta}_1 & \boldsymbol{\beta}_2\end{bmatrix}\mathbf{U} \tag{8a}$$

where $\boldsymbol{\alpha}_1\left(\in\mathbb{R}^{n\times n}\right)=-\mathbf{A}_c^{-1}\mathbf{E}_p^{-1}$; (8b)

$$\boldsymbol{\alpha}_2\left(\in\mathbb{R}^{n\times n}\right)=-\mathbf{E}_p^{-1}\left(\mathbf{S}+\dot{\mathbf{E}}_p\right); \tag{8c}$$

$$\boldsymbol{\beta}_1=-\mathbf{A}_c^{-1}\mathbf{E}_p^{-1}(\mathbf{S}+\dot{\mathbf{E}}_{\mathrm{p}})\mathbf{A}_{\mathbf{E}}; \tag{8d}$$

and $\boldsymbol{\beta}_2\left(\in\mathbb{R}^{n\times1}\right)=-\mathbf{A}_{\mathbf{c}}^{-1}\mathbf{A}_{\mathbf{E}}$; (8e)

Similar to the magnetic vector potential, the magnetic flux density **B** (=$\mathbf{B}_{\mathrm{E}}$+$\mathbf{B}_{\mathrm{C}}$) at an observed point is contributed by the EM-generated MFD $\mathbf{B}_{\mathrm{E}}$ and the EC-generated MFD $\mathbf{B}_{\mathrm{C}}$. The output $\mathbf{Y_1}$ representing the MFD at R_k point is given by (9a) where $\mathbf{V}=diag(v_j)$:

$$\mathbf{Y}_1=\begin{bmatrix}\mathbf{MV} & \mathbf{0}_{2\times n}\end{bmatrix}\mathbf{X}+\begin{bmatrix}D_r & \mathbf{0}_{2\times2}\\ D_z\end{bmatrix}\mathbf{U} \tag{9}$$

where $\mathbf{M}=\begin{bmatrix}M_{r1}\cdots & M_{ri}\cdots & M_{rn}\\ M_{z1}\cdots & M_{zi}\cdots & M_{zn}\end{bmatrix}$;

$$\begin{bmatrix}M_{ri}\\ M_{zi}\end{bmatrix}=\frac{\mu_o}{4\pi a_0}\int_{\theta=0}^{2\pi}\begin{bmatrix}\rho_a R_i\left(Z_j-Z_i\right)\cos\theta\\ R_i-R_k\cos\theta\end{bmatrix}\frac{d\theta}{\left|\mathbf{R}_k-\mathbf{R}_i\right|^3}$$

and $$\begin{bmatrix}D_r\\ D_z\end{bmatrix}=\frac{a\mu_o}{4\pi}\int_{\theta=0}^{2\pi}\int_{z=-1}^{1}\int_{r=\rho_i}^{\rho_o}\begin{bmatrix}\rho_a\left(Z_j-Z\right)\cos\theta\\ R-R_k\cos\theta\end{bmatrix}\frac{R\,dRdZd\theta}{\left|\mathbf{R}_k-\mathbf{R}\right|^3}.$$

As shown in Fig. 1(b), the MF in 2D axisymmetric coordinates passing through a coil can be regarded as the summation of MF through the rings. The outputs Y_2 and Y_3 representing the MF passes through a coil and induced EMF are given by (10) and (11) respectively:

$$Y_2=\Phi_{\mathrm{B}}=2\pi\mathbf{NR}\left(\begin{bmatrix}\mathbf{C} & \mathbf{0}_{2m\times n}\end{bmatrix}\mathbf{X}+\begin{bmatrix}\mathbf{D} & \mathbf{0}_{2m\times n}\end{bmatrix}\mathbf{U}\right) \tag{10}$$

where $\mathbf{N}\left(\in\mathbb{R}^{1\times2m}\right)=\begin{bmatrix}[n_{1x}\ n_{1y}]\cdots & [n_{kx}\ n_{ky}]\cdots & [n_{mx}\ n_{my}]\end{bmatrix}$

$$\mathbf{R}\left(\in\mathbb{R}^{2m\times2m}\right)=diag\left(\begin{bmatrix}R_ks_k & R_ks_k\end{bmatrix}\right)$$

$$\mathbf{C}=\begin{bmatrix}\mathbf{M}_1\mathbf{V}\cdots & \mathbf{M}_k\mathbf{V}\cdots & \mathbf{M}_m\mathbf{V}\end{bmatrix}^{\mathrm{T}}$$

and $\mathbf{D}=\begin{bmatrix}[D_{r1}\ D_{z1}]^{\mathrm{T}}\cdots & [D_{rk}\ D_{zk}]^{\mathrm{T}}\cdots & [D_{rm}\ D_{zm}]^{\mathrm{T}}\end{bmatrix}^{\mathrm{T}}$

$$Y_3=V_b=-N_w\dot{Y}_2 \tag{11}$$

In (10) where k=1, …, m, m is the number of segments (each with length segment s_k); [n_{kx}, n_{ky}] indicate the (x, y) components of the normal vector; and R_k is the radial position.

C. Harmonic response of ECD, MF, EMF

The harmonic solutions to the ECD fields in (7) are given in (12), which is determined by substituting $\mathbf{J}=\mathbf{J}_{\mathrm{Re}}+\mathrm{j}\mathbf{J}_{\mathrm{Im}}$ into (8), where $\mathbf{J}_{\mathrm{Re}}$ and $\mathbf{J}_{\mathrm{Im}}$ are the real and imaginary part of **J**. $\mathbf{E}_{\mathrm{PR}}=diag(\mu_0\varepsilon_{\mathrm{Re}\,j})$, $\mathbf{E}_{\mathrm{PI}}=diag(\mu_0\varepsilon_{\mathrm{Im}\,j})$, where ε_{Rj} and ε_{Ij} are the real and imaginary part permittivity.

$$\begin{bmatrix}\mathbf{J}_{\mathrm{Re}}\\ \mathbf{J}_{\mathrm{Im}}\end{bmatrix}=\begin{bmatrix}\mathrm{I}-2\omega^2\mathbf{E}_{\mathrm{PR}}\mathbf{A}_{\mathbf{C}} & \omega\left(\mathbf{S}+2\omega\mathbf{E}_{\mathrm{PI}}\right)\mathbf{A}_C\\ \omega\left(\mathbf{S}+2w\mathbf{E}_{\mathrm{PI}}\right)\mathbf{A}_C & 2\omega^2\mathbf{E}_{\mathrm{PR}}\mathbf{A}_{\mathbf{C}}-\mathrm{I}\end{bmatrix}^{-1}\times\begin{bmatrix}2\omega^2\mathbf{E}_{\mathrm{PR}}\mathbf{A}_E\\ -\omega\left(\mathbf{S}+2\omega\mathbf{E}_{\mathrm{PI}}\right)\mathbf{A}_E\end{bmatrix}J_E \tag{12}$$

Similar to the ECD fields, the harmonic response of MFD, MF, EMF are given by $\mathbf{Y}=\mathbf{Y}_{\mathrm{Re}}+\mathrm{j}\mathbf{Y}_{\mathrm{Im}}$

$$\mathbf{Y}_1=\begin{bmatrix}\mathbf{Y}_{1\mathrm{Re}}\\ \mathbf{Y}_{1\mathrm{Im}}\end{bmatrix}=\begin{bmatrix}\mathbf{MVJ}_{\mathrm{Re}}+\begin{bmatrix}D_r & D_z\end{bmatrix}^{\mathrm{T}}J_E\\ \mathbf{MVJ}_{\mathrm{Im}}\end{bmatrix} \tag{13}$$

$$\mathbf{Y}_2=\begin{bmatrix}Y_{2\mathrm{Re}}\\ Y_{2\mathrm{Im}}\end{bmatrix}=\begin{bmatrix}2\pi\mathbf{NR}\left(\mathbf{CJ}_{\mathrm{Re}}+\mathbf{D}J_e\right)\\ 2\pi\mathbf{NRCJ}_{\mathrm{Im}}\end{bmatrix} \tag{14}$$

$$\mathbf{Y}_3=\begin{bmatrix}Y_{3\mathrm{Re}}\\ Y_{3\mathrm{Im}}\end{bmatrix}=\omega N_w\begin{bmatrix}-Y_{2\mathrm{Im}}\\ Y_{2\mathrm{Re}}\end{bmatrix} \tag{15}$$

III. Numerical Verifications

The DCS method and its physical insights into modeling an induced ECD field of a biological object and its generated MFD are illustrated numerically. Since no analytical solutions are available for comparison, commercial FEA software (COMSOL) has been used as a basis to verify the DCS-modeled M/EC fields of biological tissues. Two examples are utilized to illustrate the DCS models for electromagnetic stimulation:

1) Three-layer (brain, skull, and scalp) head model [22], Fig. 2 and Table I.
2) Electrical conductivity imaging [27], Figs. 3 to 5 and Table II.

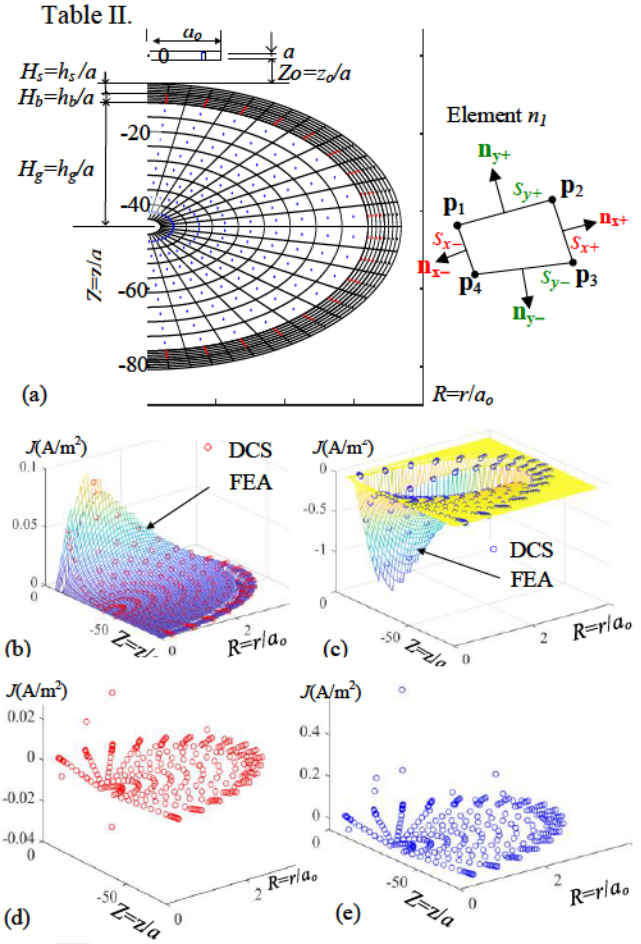

Fig. 2. Axisymmetric three-layer head model for TMS example. (a) Simulation configuration. (b, c) ECD (Re, Im) parts: DCS and FEA. (d, e) Error plots of ECD (Re, Im) parts.

In both examples, the material properties (σ, ε_r) are determined by the Cole-Cole dispersion in (1b, c). Four-vertex quadrilateral elements as shown in Fig. 2(a) were used in the simulations, where the vectors ($\mathbf{p}_1$ to $\mathbf{p}_4$) denote the vertex positions; and (s_k and n_k where k=$x_\pm$ and $y_\pm$) are the k^{th} boundary line and normal vector respectively. The 2D quadrilateral elemental areas, boundary lines, and normal vectors can be calculated from (16a~c):

$$v_i = \frac{1}{2}\left(|\mathbf{p}_2-\mathbf{p}_1||\mathbf{p}_4-\mathbf{p}_1| + |\mathbf{p}_2-\mathbf{p}_3||\mathbf{p}_4-\mathbf{p}_3|\right) \tag{16a}$$

$$\begin{aligned} s_{x+} &= |\mathbf{p}_3-\mathbf{p}_2|;\ s_{x-} = |\mathbf{p}_1-\mathbf{p}_4|; \\ s_{y+} &= |\mathbf{p}_4-\mathbf{p}_3|;\ s_{y-} = |\mathbf{p}_2-\mathbf{p}_1| \end{aligned} \tag{16b}$$

$$\begin{aligned} \mathbf{n}_{x+} &= \begin{bmatrix} p_{3y}-p_{2y} \\ p_{3x}-p_{2x} \end{bmatrix};\ \mathbf{n}_{x-} = \begin{bmatrix} p_{1y}-p_{4y} \\ p_{1x}-p_{4x} \end{bmatrix}; \\ \mathbf{n}_{y+} &= \begin{bmatrix} p_{4y}-p_{3y} \\ p_{4x}-p_{3x} \end{bmatrix};\ \mathbf{n}_{y-} = \begin{bmatrix} p_{2y}-p_{1y} \\ p_{2x}-p_{1x} \end{bmatrix} \end{aligned} \tag{16c}$$

A. ECD induced in the head model of TMS

Figure 2(a) shows the 3-layer (brain, skull and scalp) head model for TMS [20]. Modeled using the DCS method in the 2D-axisymetric coordinates, the three layers of the half-circle geometrical structure are denoted as GM (grey matter), CB (cortical bone) and WS (wet skin) in Fig. 2(a). The EM configuration and head model, along with the parametric values used in simulations, are summarized in Table I where the distance Z_o (between EM and head) is normalized to a. Figs. 2(b, c) plot the simulated real and imaginary parts of the induced ECD. The close agreements validate the DCS methods. The RMS error between the DCS method and FEA solutions is quantitatively evaluated. The RMS errors of the real and imaginary parts are 0.0031 and 0.0393 respectively. The element position of the maximum ECD (*R*, *Z*)=(0.776, −15) and its values are (0.06, 1.125) A/m^2 for the (real, imaginary) parts respectively. Fig. 2(d), (e) are the errors of real and imaginary part ECDs, which are determined by the ECD values of the DCS method subtracted from the FEA method. The relatively large differences in Fig. 2(d, e) are due to the abrupt change near the boundary of different materials.

TABLE I. Simulation Parameters of TMS for Head Model

Electromagnet (EM)			
Coil geometry (cm)		**Current**	
Inner radius, a_i	2	J_E (kA)	7.66
Outer radius, a_o	2.5	f (kHz)	3.6
Thickness, a	0.25		

Head model (Z_o=8.2)				
Geometry (normalized to a)			**Material**	
	Radius	**# of layers**	σ (S/m)	ε_r
GM	H_g 32	8	0.001069	$56950.1 - j\,534495$
CB	H_b 2.4	3	0.00203	$1080.33 - j\,101542$
WS	H_s 2.4	3	0.00106	$30373.7 - j\,5283.29$

RMS (real, imaginary) error between the DCS solutions and FEA

$$\text{RMS} = \sqrt{\frac{1}{n}\sum_{i=1}^{n}\left(y_{DCS}-y_{FEA}\right)^2}$$

RMS error (real) = 0.0031
RMS error (Imaginary) = 0.0393

B. MFD, MF and EMF for electromagnetic sensing

Figure 3(a) shows the example of electrical conductivity imaging demonstrated in [27] via contactless measurements using an excitation coil and a pair of sensing coils, where conductive solution was used to simulate the object material; and the permittivity was not considered. As an illustrative application, the experimental setup in [27] was modeled using the DCS method for electromagnetic sensing but the conductive solution was replaced by wet skin material as an example of the biological object in this study. The parametric values used to simulate this electromagnetic sensing application in Table II and Fig. 3(a). The results are summarized in Figs. 3 to 5, from which the observations can be made:

– Fig. 3(b) shows the (Re, Im) parts of the EM-generated MFD along the radius in the cross-section of Sensing Coil 1, which were computed from the analytical solutions and compared with FEA. Figs. 3(c, d) compare the (Re, Im)

parts of the ECD computed using the DCS and FEA methods. The comparisons between DCS and FEA show excellent agreements.

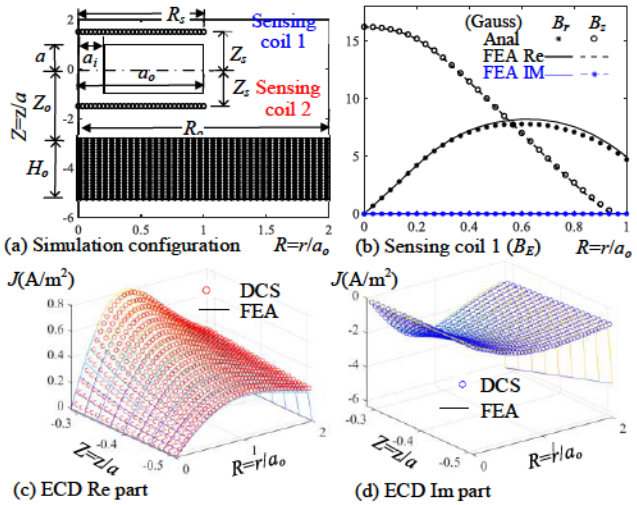

Fig. 3 Magnetic sensing example. (a) Simulation configuration. (b) EM-generated MFD (Re, Im) parts of Sensing Coil 1. (c, d) ECD (Re, Im) parts: DCS and FEA.

– Fig. 4(a) plots the (Re, Im) parts of the weak MFD generated by the ECD induced in the biological object. Fig. 4(a) is the FEA simulated Re part of the MFD contributed by the ECDs induced in the biological object, which was obtained by subtracting the EC-generated MFD simulated using FEA mesh (Fig. 4d, EM only) from that using FEA mesh (Fig. 4c, both EM and object). However, because of the large differences between the MFD generated by the EM and that by the induced ECD in the biological object, FEA fails to compute the MFD contributed by the induced ECD in the biological object.

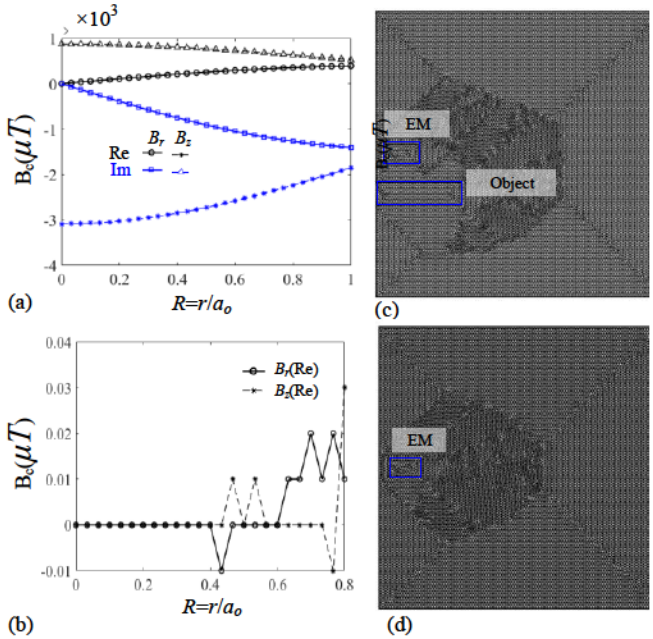

Fig. 4. Object EC-generated MFD. (a) DCS modeled MFD (Re, Im) parts. (b) FEA-modeled MFD (Re, Im) parts. (c, d) FEA meshes (with and without object) for computing object-EC MFD.

– To further compare the DCS- and FEA-modeled MFD generated by induced EC in the biological object, the electrical conductivity of wet skin is multiplied by a factor of 10^6 such that the EM-generated MFD and the EC-generated MFD are in similar order-of-magnitude. As illustrated in Fig. 5, DCS models yield smoother results as compared with FEA results.

– The EMF generated from the induced ECD of the sensing objects are investigated by (15). The EMF ($Y_{3\mathrm{Re}}$, $Y_{3\mathrm{Im}}$) of Sensing Coils 1 and 2 for the wet skin are (0.1328, 0.0375) V and (0.0552, 0.0156) V, and for conductivity solution are (1.04, –0.001) V and (2.507, –0.021) V.

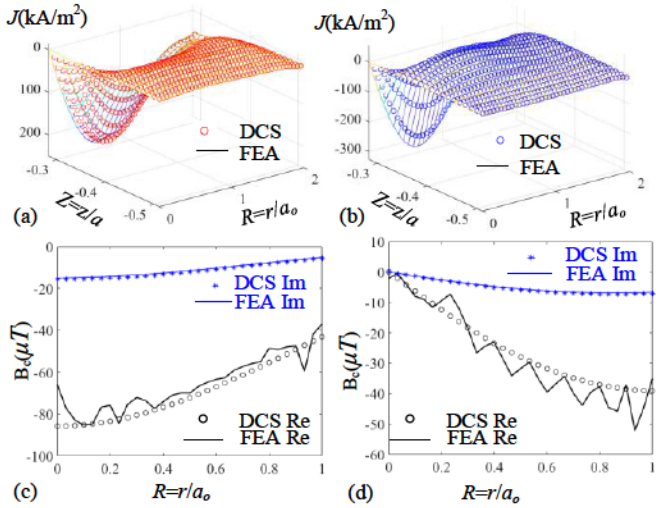

Fig. 5 Comparing DCS and FEA Simulations with electrical conductivity multiplied by a factor of10^6. (a, b) ECD (Re, Im) parts. (c, d) MFD (Re, Im) parts.

TABLE II. PARAMETRIC VALUES OF ELECTROMAGNETIC SENSING

Exciting coil			
Geometry (cm)		**Current**	
a_i	3	I_0 (mA)	200
a_o	15	f (kHz)	500
a	3.5	N_E	100

Biological object				
Normalized Geometry		**Material**		
			σ(S/m)	ε_r
Z_o	2.86	WS	0.1779	3614.5– j6403.8
R_o	2	Cond. Sol.	6.72	0
H_o	2.67			

Sensing coils		
$N_w = 10000$	$Z_s = 1.42$	$R_s = 1$

IV. CONCLUSION

The M/EC fields of the biological objects in 2D-axisymmetric coordinate are formulated in state-space representation. The DCS method is numerically verified, which agrees well with the results computed using commercial FEA software. The simulation results demonstrate the DCS method perform better than FEA for calculations of the weak MFDs generated from the tiny ECDs induced in the biological objects. The applications of the DCS method are demonstrated by two examples: the calculations of ECD fields of a multiple layer head model for TMS and EMF of the sensing coils for the electromagnetic sensing. It is expected that the DCS method has broad applications on the design analysis of bio-mechatronics systems.

Manuscript 408 submitted to IEEE/ASME International Conference on Advanced Intelligent Mechatronics. Received March 15, 2019.

REFERENCES

[1] H. A. Sodano, J.-S. Bae, D. J. Inman, W. K. Belvin, "Concept and model of eddy current damper for vibration supperssion of a beam," *Journal of Sound and Vibration*, no. 288, pp. 1177-1196, 2005.

[2] L. W. Jin, J. Zheng, H. T. Li, J.P. Li, Z.J. Zhou, Y. Zhang, and Z.G. Deng, "Effect of eddy current damper on the dynamic vibration characteristics of high-temperature superconducting maglev system," *IEEE Trans. on Applied Superconductivity*, vol. 27, No. 3, pp. 805–824. Apr. 2017.

[3] H.-L. Lin, S.-C. Chen, M.-C. Jeng, P. S. Minh, "Induction heating with the ring effect for injection mold plates," *International Communications in Heat and Mass Transfer*, vol. 39, no. 4, pp. 514-522, 2012.

[4] F. Moro and L. Codecasa, "A 3-D hybrid cell method for induction heating problems," *IEEE Trans. on Magnetics*, vol. 53, No. 6, Jun., 2017.

[5] M. R. Nabavi, S. N. Nihtianov, "Design strategies for eddy-current displacement sensor systems: review and recommendations, " *IEEE Trans. on Sensors*, vol. 12, No. 12, pp. 3346–3355. Dec. 2012.

[6] T. Yamaguchi, Y. Iwai, S. Inagak, M. Ueda, "A method for detecting bearing wear in a drain pump utilizing an eddy-current displacement sensor, " *Measruement*, vol. 33, No. 3, pp. 205–211. Apr., 2003.

[7] H. B. Wang, W. Li, and Z. H. Feng, "Nontact thickness measurement of metal films using eddy-current sensors immune to distance variation, " *IEEE Trans. on Instrumentation and measurement*, vol. 64, No. 9, pp. 2557–2564, Sep. 2015.

[8] X. Ma, A. J. Peyton, and Y. Y. Zhao, "Measruement of electrical conductivity of open-celled Aluminum foam using non-contact eddy current techniques," *NDT&E International*, vol. 38, No.5, pp. 359-367, Jul. 2005.

[9] K. –M. Lee, C.-Y. Lin, B.J. Hao, and M. Li, "Coupled parametric effects on magnetic fields of eddy-current induced in non-ferrous metal plate for simultaneous estimation of geometical parameters and electrcail conductivity," *IEEE Trans. Magnetics*, vol. 53, No. 10, Oct. 2017.

[10] E. M. Wassermann, S. H. Lisanby,"Therapeutic application of repetitive transcranial magnetic stimulation: A review," *Clin. Neurophysiol.*, vol. 112, no. 8, pp. 1367-1377, 2001.

[11] S. H. Lisanby, "Transcranial magnetic stimulation: Applications in basic neuroscience and neuropsychopharmacology," *Internataionl. Journal of* Neuropsychopharmacol., vol. 3, no. 3, pp. 259-273, 2000.

[12] Z. Zakaria, R. A. Rahim, M. S. B. Mansor, S. Yaacob, N. M. N. Ayob, S. Z. M. Mjji, M. H. F. Rahiman, and S. M. K. S Aman, "Advancements in Transmitters and Sensors for Biological Tissue Imaging in Magnetic Induction Tomography," *Sensors*, vol. 12, pp. 7126-7156, 2012.

[13] J. Netz, E. Forner, S. Haggemann, "Contactless impedance measurements by magnetic induction-A possible method for investigation of brain impedance," *Physiol. Meas.*, vol. 25, p315-323, 2004.

[14] R. Seeton, A. Adler, "Senstivity of a single coil electromagnetic sensor for non-contact monitoring of breathing", *In Proceedings of 30th Annual International Conference of the IEEE Engineering in Medicine and Biology Society*, Vancouver, BC, Canda, pp. 518-521, Aug. 2008.

[15] R. Casanas, H. Scharfetter, A. Altes, A. Remacha, P. Sarda, J. Sieera, R. Merwa, K. Hollaus, Rosell, "Measurement of liver iron overload by magnetic induction using a planar gradiometer: Preliminary human results," *Physiol. Meas.*, vol. 25, pp. 315-323, 2004.

[16] C. V. Dodd and W. E. Deeds, "Analytical solutions to eddy-current probe-coil problems," *J. Appl. Phys*., vol. 39, pp. 2829-2838, May, 1968.

[17] K.-M. Lee, L. Yang, K. Bai, J. Ji, "An efficient flexible division algorithm for predicting temperature-fields of mechatronic system with manufacturing applications," *IEEE/ASME Trans. on Mechatronics*, vol. 22, no. 4. August 2017. pp 1818-1827.

[18] J.-Y. Lim and K.-M. Lee, "Distributed multi-level current models for design analysis of electromagnetic actuators," *IEEE Trans. on Mechatronics*, vol. 20, no. 5, October 2015, pp. 2413-2424.

[19] C.-Y. Lin, K.-M. Lee, and B.J. Hao, "Distributed current source method for modeling magnetic and eddy-current fields induced in nonferrous metallic objects," *IEEE/ASME Trans. on Mechatronics,* 2017; DOI: 10.1109/TMECH. 2017.2771763.

[20] O. P. Gandhi, J. F. Deford, and H. Kanai, "Impedence method for calculation of power deposition patterns in magnetically induced hyperthermia," *IEEE. Trans. Biomedical Eng.*, vol. 31, *No*. 10, pp. 644-651, Oct., 1984.

[21] N. Orcutt, and O. P. Gandhi, "A 3-D impedence method to calculate power deposition in biological bodies subjected to time varying magnetic fields," *IEEE. Trans. Biomedical Eng.*, vol. 35, *No*. 8, pp. 577-583, Aug., 1988.

[22] N. D. Geeter, G. Crevecoeur, and L. Dupre, "An efficient 3-D eddy-current solver using an independent impedance method for transcranial magnetic stimulation," *IEEE Trans. on Biomedical Engineering*, vol. 58, No. 2, pp. 310-320, Oct., 1984.

[23] N. D. Geeter, G. Crevecoeur, and L. Dupre, "Eddy-current simulations using an independent impedance method in anisotropic biological tissues," *IEEE Trans. on Magnetics*, vol. 47, No. 10, pp. 3845-3848, Oct., 2011.

[24] K. S. Cole and R. H. Cole, "Dispersion and absorption in dielectrics: Alternating current characteristics," *Journal Chemical Physics*, vol. 9, pp. 341-351, 1941.

[25] S. Gabriel, R. W. Lau, and C. Gabriel, "The dielectric properties of biological tissues-Part III: Parametric models for the dielectric spectrum of tissues," *Physics in Medicine and Biology*, vol. 41, pp. 2271-2293, 1996.

[26] D. K. Cheng, Field and wave electromagnetics. Addison Wesley, Second Edition.

[27] B. U. Karbeyaz ve N. G. Gencer, "Electrical conductivity imaging via contactless measurements: an experimental study," *IEEE Trans. Med. Imag.*, vol. 22, no 5, 2003.